Radiation-induced segregation/precipitation in Fe-Ni and Fe-Mn model alloys: Dose rate and solute effects

L.T. Belkacemi-Rebrab, E. Meslin, J-P. Crocombette, Bertrand Radiguet, F. Leprêtre, B. Decamps

Radiation-induced segregation/precipitation in Fe-Ni and Fe-Mn model alloys: Dose rate and solute effects

L. T. Belkacemi[a], E. Meslin[a], B. Radiguet[b], J-P. Crocombette[a], F. Leprêtre[a] and B. Décamps[c]

[a] *Université Paris-Saclay, CEA, Service de Recherches de Métallurgie Physique, Gif-sur-Yvette, France*

[b] *Groupe de Physique des Matériaux, UMR CNRS 6634, Université et INSA de Rouen, 76801 Saint Etienne du Rouvray, France*

[c] *Laboratoire de Physique des 2 infinis Irène Joliot-Curie (IJC Lab), Université Paris-Saclay, Orsay, France*

Keywords: electron microscopy, atom probe tomography, ion irradiation, solute effect, radiation-induced segregation/precipitation

Abstract

The evolution of radiation damage in steels is a major issue for the safe operation of Nuclear Power Plants. Mn and Ni contribution to the formation and evolution of microstructural features remains a controversial issue. The present study aims at investigating their effects on microstructure by irradiating undersaturated BCC Fe-3.3at.%Ni and Fe-2.8at.%Mn model alloys. Two different ion irradiation conditions have been applied to study the effect of irradiation dose rate in both of these Fe-based alloys at a temperature of 673 K. In all cases, irradiation promotes the formation of dislocation loops. In the FeNi alloy, radiation-induced segregation is observed on loops, leading to precipitation of a FCC phase in the low dose rate irradiation condition only. In the case of FeMn, even if no precipitation occurred, highly enriched decorated dislocation loops are observed, leading to a higher Mn segregation at radiation defects than Ni.

1. Introduction

Reactor Pressure Vessel (RPV) steel embrittlement in Nuclear Power Plants (NPPs) is well-known to be due to the formation and evolution, under irradiation, of complexes made of point defects (PDs: vacancies and self-interstitial atoms) and solute atoms such as Cu, Si, Mn, Ni and P, that impede dislocation motion [1–5]. Such evolution at nm-scale plays a key role upon the microstructure and the resulting mechanical properties.

Under irradiation, PDs in excess can drag solutes towards PD sinks due to flux coupling. This is the so-called Radiation-Induced Segregation (RIS) mechanism [6] that can occur even in undersaturated alloys. This atomic diffusion process can be very efficient due to the permanent excess of PDs, regardless of whether thermodynamic driving forces act on the system or not. Mechanisms leading to the formation of these clusters have yielded a huge amount of theoretical and experimental studies over the past 40 years [7–19], showing the singularity of each solute constituting RPV steels [20,21]. The first element that gained attention among the scientific community is copper [22–24]. In steels with low Cu contents, such as French RPVs, Cu migration towards PD sinks (vacancy clusters and interstitial clusters) is covered by vacancies [7,25–28]. At the opposite, for phosphorous, the predominant contribution to this solute diffusivity is provided by mixed dumbbells [29]. Therefore, the understanding of segregation mechanisms occurring under irradiation is not straightforward but still a challenging problem. In 1995, the possibility of forming MnNi-rich clusters was put forward by G. R. Odette et al. [30]. The authors then demonstrated by Lattice Monte Carlo (LMC) simulations the MnNi precipitates

complex chemical structures that can form depending on Cu, Ni and Mn contents and temperature [26]. Studies made on Cu-core-MnNiSi-shell, Cu-core-MnNiSi-appendage precipitates and MnNi clusters in low Cu and Cu-free alloys, showed that these clusters play the dominant role in the hardening and embrittlement of the materials of interest [31,32]. As a result, the question of the mechanisms leading to the formation of these MnNi-rich clusters/precipitates was raised. L. Messina et al. [29,33] demonstrated that the positive coupling between Ni atoms and vacancies leads to an enrichment in Ni in the vicinity of PD sinks, up to a temperature of 1087 K. In the case of Mn, coupling with both the interstitials (formation of Fe-Mn mixed dumbbells), and vacancies lead to Mn enrichment in the vicinity of PD sinks up to a temperature of 1011 K. However, even though solute dragging by PDs, namely RIS, is known to be a strong mechanism for solute enrichment or depletion on microstructural defects, to date, the driving force for their clustering is still a matter of debate [34].

On the one hand, these MnNi clusters (MNSs and MNSPs when containing Si and Si-P atoms respectively) are called "Late Blooming Phases" (LBP) [21]–[23]. They are claimed to be thermodynamically stable, to form at high neutron fluence then grow rapidly, leading to an accelerated embrittlement of the steel [38]. Under this assumption, RIS is believed to play a role in MNSP formation, especially in the nucleation stage (segregation on small dislocation loops created in displacement cascades), after which precipitation of phases such as G ($Mn_6Ni_{16}Si_7$) and Γ_2 (Mn_2Ni_3Si) phases [39,40] takes place. In that respect, S. Shu et al. [41] recently developed a kinetic lattice Monte Carlo method, parameterized using CALPHAD and recent APT data to simulate post-irradiation annealing (PIA) of MNSPs. The results showed a good agreement with experimental observations, in terms of volume fractions, number densities and sizes. It also predicts the initial structure of the MNS precipitates as B2 bcc stable phases. Further 425°C PIA experiments were conducted in intermediate and high Ni RPV steels irradiated to a high fluence with neutrons at ≈320°C [42]. The authors showed MNSP precipitate coarsening by Atom Probe Tomography (APT) and Scanning Transmission Electron Microscopy (STEM), suggesting their stability even at a temperature 105°C higher than their formation temperature. These phases are thus believed to be stable at the operating temperature of ≈290°C.

On the other hand, similar experimental works were performed by E. Meslin et al. [43] on a neutron-irradiated Fe1.1Mn0.7Ni (at.%) alloy subjected to a 400°C PIA. They revealed a partial dissolution of MnNi clusters. Even though a possible synergistic effect between Mn and Ni is plausible, Mn and Ni segregation is suggested to result from a radiation-induced mechanism **only** and are, thereby, considered as unstable. These observations were supported by atomistic simulations reporting a very early nucleation of Mn-Ni-rich clusters growing much slower than Cu-rich clusters [44]. Density functional theory (DFT) calculations and Monte Carlo simulations performed by G. Bonny et al. [45] revealed the unstability of Mn–Ni pairs and triplets but an attractive binding energy after their clustering, reinforcing the assertion of the induced mechanism as being the only one acting on solutes.

Along with solute clustering mechanisms, we address the issue of laboratory experience transferability. In the literature, most of experimental works are based on irradiation campaigns involving experimental reactors (with a dose rate 10 to 100 times higher than in NPPs) or charged particle accelerators (ions or electrons, with a dose rate 1 to 10 million times higher than in NPPs). The use of charged particle accelerators is justified by their accessibility, their lower cost and the absence of radioactivity in samples, making the post-irradiation analysis much easier to handle. Moreover, using higher dose rates enables a significant reduction of materials exposition time. In that respect, the dose at which is subjected a RPV steel after 40 years can be achieved within few minutes only. Irradiation conditions (temperature, dose and dose rate) can be properly controlled.

In this context, solute clustering mechanisms and dose rate effects were investigated concomitantly by characterizing the microstructure of Fe-3.3at.%Ni and Fe-2.8at.%Mn model alloys, irradiated up to a dose of 1.2-1.9 and 1.9-2.3 dpa respectively, using two different dose rates for each alloy. These materials allow investigating the behavior of two solutes of importance in RPV steels ageing, avoiding synergistic effects with other solutes (Cu, Si, P, Mo, etc.) and simplifying the microstructure (fully ferritic materials).

The solute content (nearly 3 at.%) was deliberately chosen higher than that in RPV steels (between 0.4 and 0.8 at.% Ni and between 1.2 and 1.5 at.% Mn [46]), in order to emphasize the mechanisms associated to solute diffusion under irradiation. However, materials remain undersaturated, so that RIS is assumed to be the only mechanism at the origin of solute clustering. They will be referred to as Fe3%Ni and Fe3%Mn along this publication.

The paper is structured as follows. Section 2 describes the methodology applied to address the questions developed above. Results obtained in the Fe3at.%Ni and Fe3at.%Mn alloys irradiated at two different dose rates are presented in section 3. A discussion is conducted in section 4 to assess the segregation mechanism, the effects of dose rate on irradiation damage, as well as the alloying effect.

2. Method

2.1. Materials

Materials used in this work are high-purity BCC FeNi and FeMn model alloys. At the temperature of interest in this study (673 K), they constitute a solid solution where solute atoms are homogeneously distributed in the Fe matrix. They were elaborated at Ecole des Mines de Saint-Etienne (EMSE, France). The furnisher also performed chemical analyses using Atomic Absorption Spectroscopy (AAS) for Ni and Mn and combustion analysis for C, O, N and S. The obtained chemical compositions are given in Table 1.

Table 1: Chemical composition of the Fe3at.%Ni and Fe3at.%Mn alloys, as received from EMSE (nominal composition). Balance is Fe.

	Ni (at.%)	Mn (at.%)	C (appm)	S (appm)	O (appm)	N (appm)
Fe3at.%Ni	3.3	--	< 23	< 4	< 35	< 4
Fe3at.%Mn	--	2.85	< 21	< 14	< 3	< 5

The materials were hot forged and thermally treated at 1173 K during 16 hours under a pure Argon flow. The latter step is of high importance in order to recrystallize the material and obtain a large grain size (> 100 µm) and a low dislocation density (~ 10^8 cm^{-2}). We evaluated the first parameter by taking SEM micrographs, and the second one using the line intercept method [47] from a TEM sample.

Both alloys were received as cylindrical rods of 10 mm in diameter and 250 mm in length. Cylinders were cut into 1 mm thick slices and mechanically polished until reaching a thickness of 0.1 mm. Then, 3 mm disc specimens were punched from the thinned slices. Before proceeding to the irradiation, a 10 seconds electropolishing step was necessary in order to remove the top layer hardened during the cold work. The electrolytic solution was made of 95% methanol and 5% perchloric acid, used at a temperature of 233 K by means of a TenuPol-5 electropolishing equipment model from Struers. The voltage was chosen equal to 23 V.

After irradiation, we used a dual-beam (Focused Ion Beam: FIB) FEI Helios NanoLab 650, located at the CEA of Saclay, to take thin foils and nanometric tips out from the bulk specimens by lift-out, for TEM and APT analyses respectively.

2.2. Irradiation conditions

The samples were irradiated at the JANNuS-Saclay facility [48,49], at 673 K, using two different irradiation conditions, referred to as high and low dose rate. In both cases, ion energy was chosen to obtain the targeted dose of 1.2 dpa sufficiently far from both the surface and the damage peak.

Dose and ion implantation depth profiles were obtained by SRIM calculations [50,51], in quick damage mode using a displacement threshold energy of 40 eV. Profiles are given in Fig. 1. The depths of observation for both irradiation conditions are indicated with hatched areas.

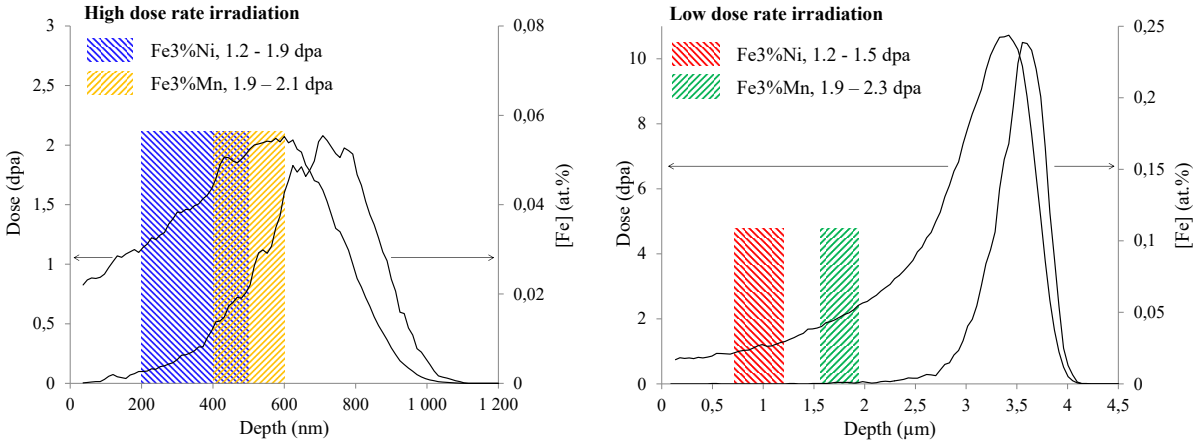

Figure 1: Dose (dpa) and ion implantation depth profile ([Fe] (at.%)) obtained in the Fe3%Ni and Fe3%Mn samples, irradiated at high dose rate (left) and low dose rate (right), estimated from SRIM calculation in "quick calculation" mode [50,51]. The sampling depth is indicated with hatched areas.

One can notice in Fig. 1 that in the Fe3%Ni alloy, the analysis was performed at 1.2-1.9 dpa. For the high dose rate condition, the corresponding depth and dose rate are 200-500 nm and 5.1 - 6.1 x 10^{-4} dpa.s^{-1}. For the low dose rate condition, the corresponding depth and dose rate are 800-1200 nm and 6.1 – 8.2 x 10^{-6} dpa.s^{-1}. The difference in dose rate is around 70.

In the Fe3%Mn alloy, the analysis was performed at 1.9 – 2.3 dpa. For the high dose condition, the corresponding depth and dose rate are 400-600 nm and 6.9 - 8.8 x 10^{-4} dpa.s^{-1}. For the low dose rate condition, the corresponding depth and dose rate are 1600-1900 nm and 1.2 – 1.5 x 10^{-5} dpa.s^{-1}. The difference in dose rate is around 60.

The analyses performed on the irradiated Fe3%Mn refer to a higher dose ranging between 1.9 and 2.3 dpa. Several trials have been attempted on tips extracted at a depth of ~200 nm (as in Fe3%Ni) so both alloys would be exactly comparable in terms of dose, in vain. For this reason, the Fe3%Mn alloy characterization was made at higher depth, dose and dose rate, compared to the Fe3%Ni alloy. The difference in dose being anyway almost similar, solute effects can still be inferred in this work.

To achieve such a high difference in dose rate (60-70), it was necessary to adjust the ion energy, yielding a possible difference in the size of cascades and sub-cascades created by individual energetic ions. It is even more true in the case of the Fe3%Mn alloy irradiated at high dose rate, where the analysis was carried out near the damage peak. A bias related to the difference in the number and size of aggregates remaining in cascades after the system relaxation can be induced. A direct consequence is the various density of nuclei (interstitial and vacancy clusters), thus PD sinks, from one condition to another. In order to estimate the effect of ion energy on nuclei density, we used the IRADINA code [52,53]. Fig. 2 gives, for each dose alloy, the proportion of each cascade according to its size, i.e. its number of defects, presented by classes of 100 defects [10-100], [101-200], [201-300], [301-400], etc. Defects containing less than 10 point defects are considered as isolated defects. Calculations were made considering a depth of 300 - 400 nm and 0.9 – 1.2 µm in the high and low dose rate irradiated Fe3%Ni specimens respectively; and a depth of 500 - 600 nm and 1.5 – 1.8 µm in the high and low dose rate irradiated Fe3%Mn specimens respectively.

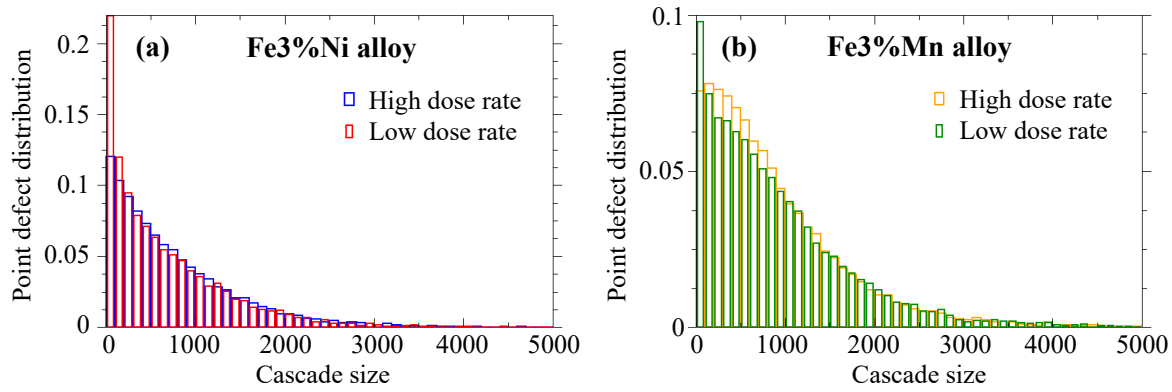

Figure 2: Proportion of each cascade size according to its number of point defects, in (a) the Fe3%Ni alloy, where the results for the high and low dose rates conditions are shown is blue and red respectively; and (b) the Fe3%Mn alloy, where the results for the high and low dose rates conditions are shown is orange and green respectively. Results were obtained using the IRADINA code [52,53].

Fig. 2 shows that the cascade distribution is quite similar for both irradiation conditions and both alloys. The major difference regards the Fe3%Ni alloy, where the low dose rate irradiation induced small cascades (between 10 and 100 PDs) which are twice as numerous as ones formed under high dose rate irradiation. The difference between the others does not exceed 8 %. In the Fe3%Mn, small cascades (between 10 and 100 PDs) are 23% more numerous in the low dose rate irradiated specimen whereas larger cascades (between 100 and 900 PDs) are slightly more frequent, with a difference of 12% at most. We therefore consider that both conditions are comparable in terms of ballistic damage. The obtained results can be attributed to dose rate effects only.

2.3. Characterization techniques

As mentioned in section 2.1, a FEI Helios NanoLab 650 FIB was used to elaborate TEM thin foils and APT needles. When a specific crystallographic orientation was seeked for further analysis, Electron Backscattered Diffraction (EBSD) maps, obtained with the same equipment, were recorded prior to the sample lift-out.

Before and after irradiation, microstructures were characterized by TEM. Chemical features were analyzed by STEM/EDS, STEM/EELS and APT.

Regarding the microstructural investigations, we used a conventional FEI 20 G_2 Tecnai TEM (CEA Saclay, France), equipped with a LaB_6 source delivering 200 keV electrons. Voids were studied by taking through-focal series images [54]. Conventional Bright Field (BF) imaging mode was used to estimate dislocation loop size. We determined their Burgers vector from micrographs recorded with various reciprocal lattice vectors **g**, by applying the **g**.**b**=0 dislocation invisibility criterion [47,55]. Especially after high dose rate irradiation condition, radiation-induced nanometric dislocation loops were small and in high density, making their individual tracing impossible when tilting to a desired diffraction condition. Therefore, the statistical method developed by A. Prokhodtseva et al. [56] was applied to estimate the loop number density. A minimum of four g vectors must be considered, with at least one non-coplanar. This method allows the determination of number densities of defects with $\frac{1}{2}a_0$<111> and a_0<100> Burgers vector and, therefore, their ratio.

Specimen thickness was estimated by STEM/EELS using the log-ratio model [57], by means of a Cs probe-corrected FEI Titan TEM (Ecole Centrale de Paris, France). Chemical investigations were carried out by STEM/EDS mostly to highlight the spatial correlation between microstructural defects and chemical heterogeneities. First, images were recorded using the High Angle Annular Dark Field (HAADF) detector. Then, the composition on several points and lines was measured by applying the Cliff-Lorimer procedure [58], with Cliff-Lorimer factors being computed from standard X-ray spectroscopic data.

To obtain more precise values of chemical concentration, APT [59,60] was used as a complementary technique. A CAMECA LEAP 4000X HR (CEA Saclay) was used in laser mode so as to increase statistics. Pulse repetition rate and base temperature were 200 kHz and 50 K respectively. For each tip, the laser pulse energy was set to an equivalent evaporation fraction of 20%. The collected data have been processed using the "GPM 3D soft" software developed in the Group of Physics of Materials (GPM, University of Rouen). First, as-received materials were analyzed and the random distribution of solute atoms was verified using X^2 statistical tests. Then, in irradiated specimens where chemical heterogeneities were highlighted, each cluster has been analyzed individually using the isoposition method (IPM) on the basis of the local solute concentration [60,61].

The concentration threshold was defined by the user by calculating the binomial distribution in a random solid solution containing a similar solute content. The solute content value corresponding to 5% of the maximum frequency was used as threshold. In the present study, the value of 9at.% was used for both alloys. Consequently, all atoms located in positions exhibiting a local solute concentration higher than 9at.% were filtered and considered as belonging to the same solute-rich cluster if the distance between them in less than 0.5 nm. In order to exclude matrix fluctuations, only clusters containing more than a minimum number of solute atoms were kept.

Thereafter, cluster elemental analysis was done taking into account atom probe artifacts. According to data obtained experimentally or calculated from field evaporation theoretical models [62], Ni evaporation field is similar to that of Fe, contrary to Mn [63]. The latter being a low field element with respect to Fe, an overdensity is expected on the detector, on positions corresponding to Mn rich atmospheres. Some Fe atoms surrounding the cluster may strike the detector at (x,y) positions corresponding to cluster atom positions and not to the interface with the matrix, inducing a biased estimation of the local concentration, as it is the case in the FeCu system [64]. These trajectory overlaps and local magnification effects have also been observed by I. Mouton et al. on Mn-rich nanocolumns distributed in a Ge matrix [65]. Raw values of Mn content are, thus, underestimated and should be corrected by removing the contribution of Fe atoms artificially introduced in Mn clusters. Therefore, an approach has been developed based on measurement of the atomic density in the cluster compared to its respective theoretical value, to better assess the local chemical composition. We corrected Mn content in this study by applying the following relation:

$$C_{Mn} = \left(C_{Mn}^{*} * \frac{\rho}{\rho_0}\right) - \left(\frac{C_{Mn}^{matrix} * (\rho - \rho_0)}{\rho_0}\right)$$

where C_{Mn}^{*} is the measured Mn content in the cluster of interest, C_{Mn}^{matrix} is the Mn content in the matrix, ρ is the cluster volume density and ρ_0 the theoretical value of Fe-α volumic density, equal to 0.085 $Å^{-3}$.

Nevertheless, this equation counts only for trajectory overlap and does not consider the local magnification effects which increase the local density without modifying chemical composition. Thus, the corrected Mn content deduced from this relation is overestimated and the actual Mn content lies between the measured and the corrected Mn content.

When possible, the solute segregated/precipitated atomic fraction was defined as the ratio between the number of solute atoms inside the clusters and the total number of solute atoms collected during the APT analysis. This value was determined in order to quantify the precipitation advancement.

3. Results and discussion

3.1. Irradiated Fe-Ni alloy

This paragraph describes the results obtained by TEM and APT in Fe3%Ni irradiated under high and low dose rate conditions, at a dose of 1.2 – 1.9 dpa.

High dose rate

As mentioned in section 2.2, the high dose rate irradiated Fe3%Ni sample was analyzed at a depth ranging between 200 and 500 nm, where the dose rate corresponds to 5.1 - 6.1 x 10^{-4} dpa.s^{-1}.

The specimen exhibits a high density of small dislocation loops but no voids. Fig. 3 presents BF TEM images taken in (101) and (001) zone axes on a FIB-elaborated lamella.

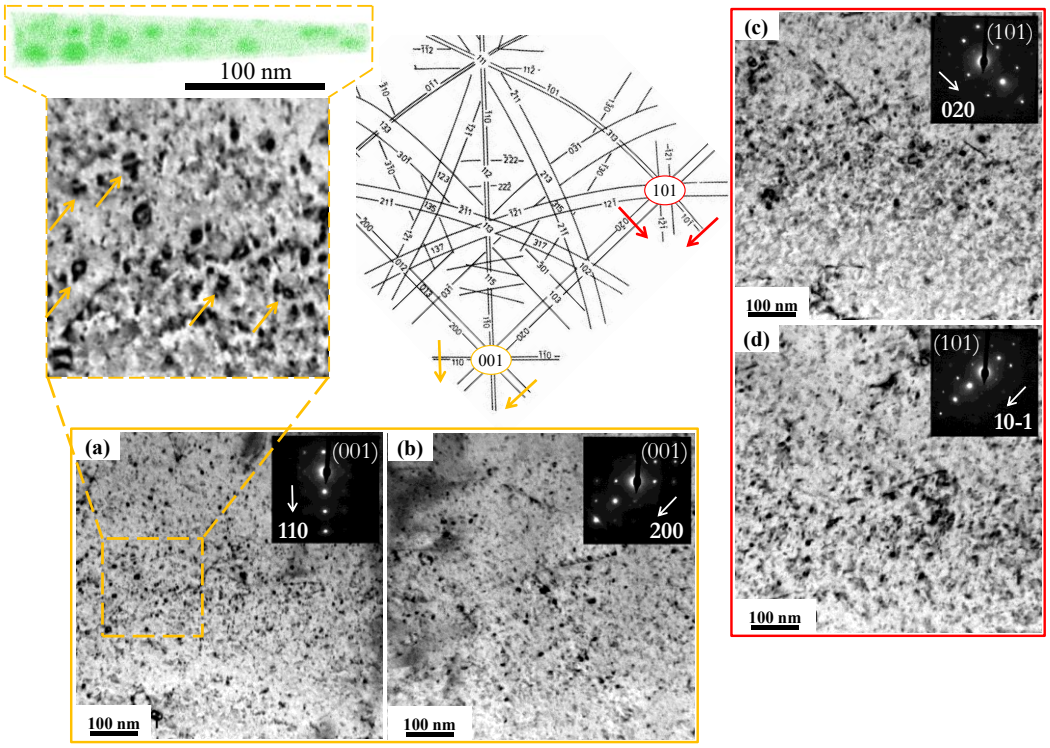

(e)

Table of visibility (V = visible, I = invisible)	Zone axes	(101)		(001)	
	g / Possible b	[020]	[10-1]	[200]	[110]
	[100]	I	V	V	V
	[010]	V	I	I	V
	[001]	I	V	I	I
	½ [111]	V	I	V	V
	½ [-111]	V	V	V	I
	½ [1-11]	V	I	V	I
	½ [11-1]	V	V	V	V

Figure 3: Central Kikuchi map extracted from [66] used to image dislocation loops formed in the Fe3%Ni sample irradiated at high dose rate. BF TEM images of dislocation loops are shown in: (a) (001) zone axis using **g**=[110]; (b) (001) zone axis using **g**=[200]; (c) (101) zone axis using **g**=[020]; (d) (101) zone axis using **g**=[10-1]. (e) Table of visibility for small dislocation loops visible on (a, b, c, d) based on **g.b** value. A magnified image of (a) is also given to provide a better view of loops, where a scaled APT reconstructed volume is also reported for comparison.

In this sample, it was not possible to trace each dislocation loop (section 2.3). Therefore, the proportion of a_0 <100> and ½ a_0 <111> loop type was estimated by resolving the equation system

arising from the invisibility criterion (table presented in Fig. 3.e). Indeed, assuming that each family form in the same proportion for each Burgers vector type [56], one can write:

If **g** = [020]

$$\frac{1}{3}d_{100} + d_{111} = A = 8.0 * 10^{21}\ m^{-3}$$

If **g** = [10-1]

$$\frac{2}{3}d_{100} + \frac{1}{2}d_{111} = B = 1.38 * 10^{22}\ m^{-3}$$

If g = [200]

$$\frac{1}{3}d_{100} + d_{111} = C = 1.33 * 10^{22}\ m^{-3}$$

If **g** = [110]

$$\frac{2}{3}d_{100} + \frac{1}{2}d_{111} = D = 1.97 * 10^{22}\ m^{-3}$$

where d_{100} is the total density of <100> type dislocation loops, d_{111} the total density of ½<111> type loops ; A, B, C and D represent the number density of visible loops under each diffraction condition.

The total number density obtained is equal to 2 ± 0.6 x 10^{22} m^{-3}, with a majority of <100> type loops (88%). The mean diameter is equal to 3 ± 1 nm, where the uncertainty is the dispersion of dislocation loop size.

APT was used to bring more information about the spatial distribution of Ni atoms. Three tips were analyzed. The example of a volume containing Ni-rich clusters is given in Fig. 3.a. Mean diameter and number density of Ni-rich clusters are respectively equal to 10 ± 3 nm and 1.4 ± 0.2 x 10^{23} m^{-3}. These clusters contain 17.0 ± 0.3 at.% on average and the segregated atomic fraction is equal to 5.2%.

Low dose rate

As mentioned in section 2.2, in the low dose rate irradiated specimen, the corresponding depth and dose rate are 800-1200 nm and 6.1 – 8.2 x 10^{-6} dpa.s^{-1}. Results obtained in this sample are reported in [67]. We recall them briefly below.

A BCC-FCC phase transformation occurred under irradiation, leading to the formation of FCC elongated precipitates, oriented along the four <111> directions of the BCC matrix (Fig. 4, redrawn from [67]). Elemental analysis, performed by APT, STEM/EDS and STEM/EELS, revealed a Ni content close to 25at.%. FCC precipitates may, therefore, correspond either to a disordered Fe25%Ni alloy or a Fe_3Ni intermetallic compound.

Considering the fact that Fe25%Ni precipitates are oriented along the <111> directions of the BCC matrix, an elemental study was conducted by APT in the same orientation, in order to intercept a precipitate all along the evaporation direction of the tip. To achieve this experiment, an EBSD map was recorded where blue, red and green grains correspond to <111>, <001> and <101> directions along z axis, perpendicular to the sample surface. Therefore, grains of interest are the ones which are oriented along the <111> directions, exhibiting one family of precipitates oriented normally to the surface. Results are presented in Fig. 4. The tip was extracted at a depth of 1.2 µm, corresponding to a dose rate of 8.5 ± 2.1 x 10^{-6} dpa.s^{-1} and a dose of 1.3 ± 0.3 dpa. The corresponding mean diameter and number density, using TEM and APT, are given in Table 2.

Under the low dose rate condition, the precipitated atomic fraction is equal to 66.2%.

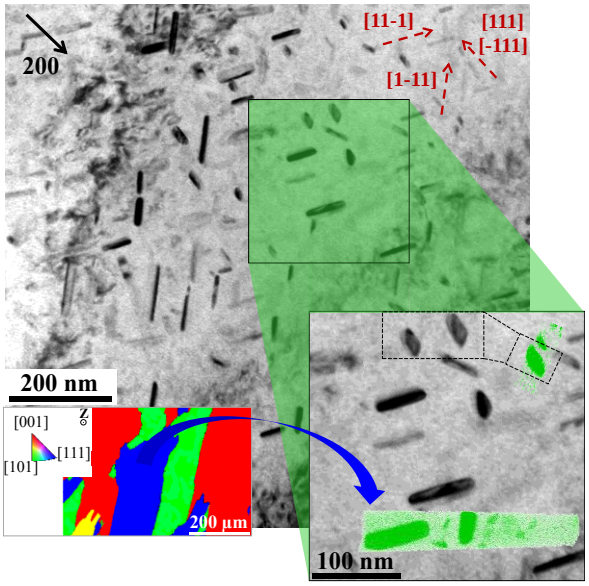

Figure 4: TEM image of the low dose rate irradiated Fe3%Ni alloy, taken in a (011) zone axis along **g**=[200], presenting elongated precipitates and scaled APT reconstructed volumes showing Ni-rich clusters (on the top and the bottom of the magnified image). The EBSD map recorded before the extraction of the tip presented is also given at the bottom-left.

Summary for the Fe3%Ni alloy

Table 2 summarizes all the data obtained in the study of Fe3%Ni irradiated at high and low dose rate.

Table 2: Results obtained in the Fe3%Ni alloy, regarding PD clusters by TEM and solute clusters by APT, after irradiation at high and low dose rates, for a same dose of 1.2 – 1.9 dpa.

Solute clusters (APT)	**High dose rate**	**Low dose rate**
Mean diameter (nm)	10 ± 3	Elongated precipitates [a]
Mean number density (x 10^{22} m^{-3})	14 ± 2	2.0 ± 0.7
Solute content (at.%)	17.0 ± 0.3	~ 25
Segregated/precipitated atomic fraction	5.2	66.2
PD clusters (TEM)	**High dose rate**	**Low dose rate**
Mean diameter (nm)	3 ± 1	48 ± 10 [b]
Mean number density (x 10^{21} m^{-3})	20 ± 6	1.6 ± 0.3

[a] Due to their large size and shape, they cross the edge of the tip.

[b] This value corresponds to the mean length of elongated precipitates.

3.2. Irradiated Fe-Mn alloy

This section is devoted to the effect of irradiation dose rate in the Fe3%Mn alloy at a dose of 1.9 – 2.3 dpa, studied by TEM and APT.

High dose rate

As mentioned in section 2.2, the high dose rate irradiated Fe3%Mn sample was analyzed at a depth and dose rate of 400-600 nm and 6.9 - 8.8 x 10^{-4} dpa.s^{-1} respectively.

In this specimen, a high density of small dislocation loops is observed, as shown in Fig. 5. No void is present. The irradiated zone is recognizable by the presence of a highly damaged strip located at a depth ranging from 400 to 700 nm. At this depth, one can notice that, at a fine scale (tens of nanometers, on the magnified TEM image), the dislocation loop density is not completely homogeneous; loop-free zones exist. The APT tip, taken out at a depth of 500 nm and presented on the top of Fig. 5 exhibits, near the apex, a small zone where no Mn-cluster is visible. Mn-rich clusters are present starting from 50 nm far from the tip surface. Therefore, at the scale of the APT tip, some defect free zones exist, as for loops and Mn clusters.

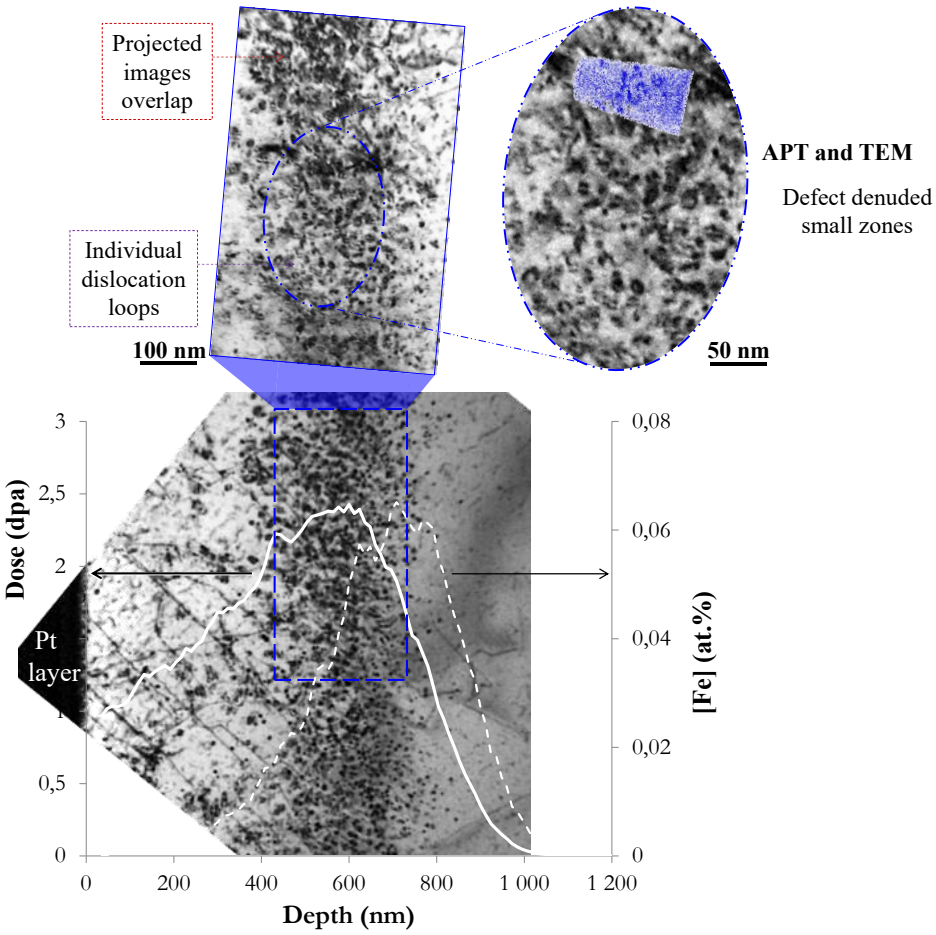

Figure 5: TEM image of dislocation loops formed in the high dose rate irradiated Fe3%Mn. The SRIM profile showing the evolution of the dose and the concentration of injected interstitials according to the depth are superimposed. A magnified image is also displayed on the top to indicate the presence of defect-free small zones (TEM and APT); of individual and overlapping loops.

Fig. 5 also shows that the projected images of dislocation loops overlap at 400 – 600 nm (depth of interest), making the determination of their Burgers vector and number density not possible. The number density, estimated over three TEM images, is however higher than 10^{23} m^{-3}. Concerning their size, the diameter does not vary according to the depth (between 400 and 600 nm). The mean value is equal to 11 ± 3 nm, where the uncertainty corresponds to the dispersion of all the measured values of diameter.

Fig. 6 shows the 3D reconstruction of one analyzed volume, where small Mn-rich clusters are present. The figure also reveals that these clusters are planar and have preferential orientations: their habitat plane forms an angle of nearly 45° with the evaporation direction of the tip, which is a <110> direction as indicated in the figure (see the black and red arrows on the left). This strongly suggests that these planar Mn-rich clusters are contained in {100} type planes, consistently with <100> dislocation loop type.

Their mean diameter is equal to 5.0 ± 0.7 nm. This value corresponds to the maximum dimension of the feature, namely in the plane. Their number density is equal to 2.9 ± 0.4 x 10^{23} m^{-3}. These values are quite different from those measured by TEM. As presented in section 2.3 referring to the difference in evaporation field between Fe and Mn, local magnification effects and ion trajectory aberrations are expected to affect the distribution of Mn atoms. Consequently, the reconstructed volume may not reflect the actual shape and concentration of Mn clusters. In terms of number density, small dislocation loop overlap observed by TEM is consistent with a large density, as demonstrated through the APT analysis (superior to 10^{23} m^{-3}). This point is explored further in section 4.1.

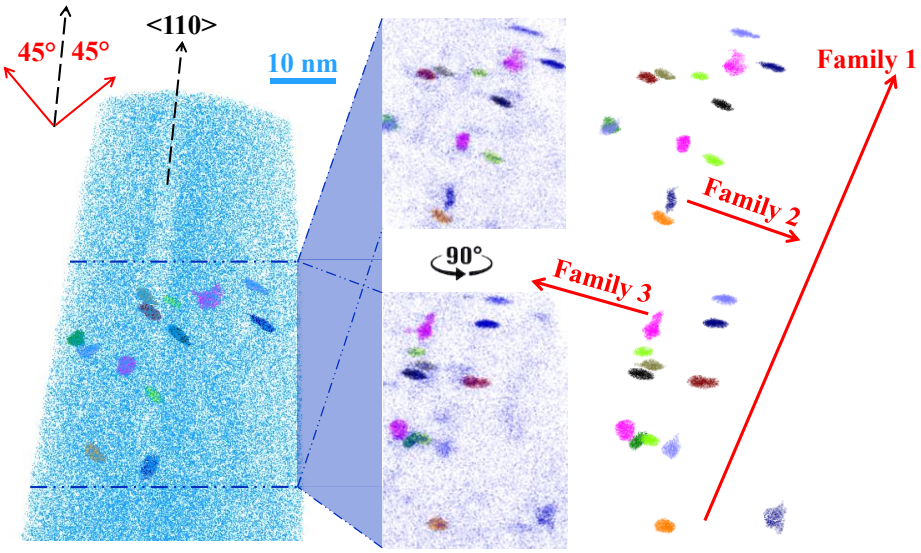

Figure 6 : 3D reconstructed volume of 50 x 50 x 120 nm^3 of high dose rate irradiated Fe3%Mn sample. Two orientations of the tip are shown and, for each, two images are presented: one with Mn matrix atoms (in blue) and the other without, so as to better distinguish colored Mn clusters. The three families of <100> dislocation loops are indicated with arrows. The z-direction goes along the evaporation direction of the tip.

For each cluster orientation, Mn content was measured. In Fig. 6, Mn clusters exhibiting different orientations are highlighted with red arrows (families 1, 2 and 3). They were chosen as they are clearly visible and large. To investigate a possible effect of orientation on evaporated ion trajectory at the interface cluster/matrix, the Mn atom density was calculated in 10 clusters belonging to different families. No correlation was found. Since an overdensity is expected, two values of mean Mn content are given: one considering only 35 Mn-clusters exhibiting an actual overdensity, a second one considering all the 48 Mn-rich clusters. For each one, the formula presented in section 2.3 was applied. As indicated in the same section, this equation does not take into account local magnification effects, which induce an overdensity without modifying the chemical composition. The corrected value is therefore overestimated: the mean Mn content in clusters lies between the measured value and the corrected value.

If only Mn clusters exhibiting a density ratio higher than 1 with the matrix are considered, the mean Mn content ranges between 26.7 ± 5.9 at.% and 38.5 ± 2.4 at.%.

If all Mn-rich clusters are considered, the mean Mn content ranges between 27.7 ± 5.4 at.% and 33.8 ± 2.4 at.%. These values are chosen as actual ones.

The segregated Mn atomic fraction, which is not expected to suffer from any local magnification effect, is equal to 9.5%.

Low dose rate

The low dose rate irradiated Fe3%Mn sample was analyzed at a depth and dose rate of 1600-1900 nm and 1.2 – 1.5 x 10^{-5} dpa.s^{-1}.

TEM investigations of the Fe3%Mn sample irradiated at low dose rate revealed the presence of a dislocation network, small dislocation loops and voids.

Fig. 7 presents TEM images, taken in bright field (center and top-left) and weak beam (bottom-left) modes with a <110> **g** vector. Two families of <100> type dislocation loops (white arrows) appear edge-on and perpendicular to the <100> directions. Their mean diameter is equal to 81 ± 26 nm, where the uncertainty corresponds to the size dispersion. Their number density is equal to 6.9 ± 0.7 x 10^{20} m^{-3}. This value takes into account the third family (on the image plane) which should not be visible under this diffraction condition, according to the invisibility criterion [47].

Smaller dislocation loops are also observed (red arrows). Their mean diameter is equal to 41 ± 6 nm and their number density to 1.3 ± 0.8 x 10^{20} m^{-3}. Here again, the number density value takes into account the invisibility criterion. These loops are very likely ½ <111> ones, since their habit plan is perpendicular to <110> direction. A magnified image presented on the upper left corner shows some of these <111> loops.

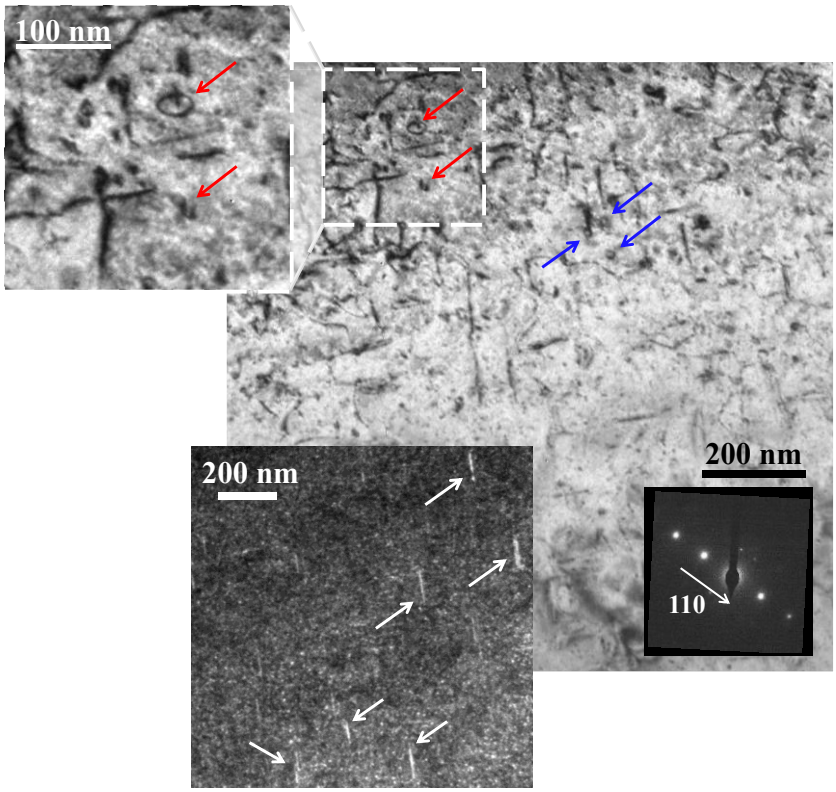

Figure 7: TEM images of the Fe3%Mn sample irradiated at low dose rate, taken in a {001} zone axis, along g = <110>, in BF mode. A magnified image is presented on the upper-left corner to highlight the presence of small ½ <111> dislocation loops, in addition to large <100> ones appearing edge-on (on the WBDF image, presented on the lower-left corner).

APT analyses were carried out on this material. Even though the dose does not correspond to the one related to TEM analysis, it revealed the presence of Mn-enriched features. Fig. 8 presents two Mn-rich clusters, highlighted by isosurfaces delimiting area with Mn concentrations higher than 7.4 at.%.

The toroidal shape of the first feature (upper part) strongly suggests that this cluster is associated with a small dislocation loop (~ 9 nm). Only a part of this feature is visible due to its position on the edge of the analyzed volume. The Mn content in the core is equal to 9.8 ± 2.8 at.%. The second feature may, due to its elongated shape, be associated to a dislocation line or a large dislocation loop. It is enriched up to 56.8 ± 5.2 at.% in the core. Since no over atom density is associated to these features, the reported composition is the measured one, without any correction. The number density of Mn-enriched feature is equal to $1.7 \pm 1.2 \times 10^{22}$ m^{-3}.

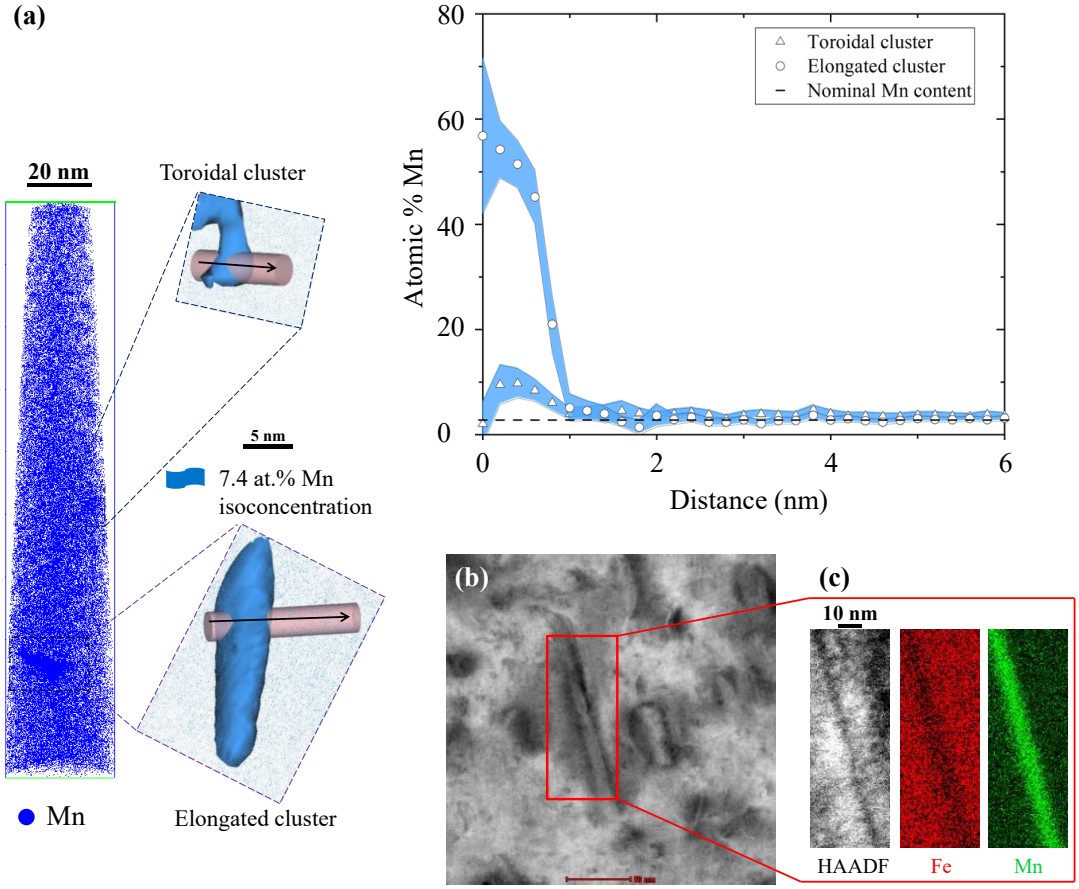

Figure 8 : (a) 3D reconstruction of an APT tip taken out from the low dose rate irradiated Fe3%Mn sample (40 x 40 x 180 nm^3). The analysis has been performed at a depth of ~1 µm, where the dose rate is $7.6 \pm 1.9 \times 10^{-6}$ dpa.s^{-1} and the dose 1.2 ± 0.3 dpa. The two Mn-rich clusters are shown next to the Mn profile measured along the brown region of interest (black arrow). (b) STEM/BF image of a dislocation loop observed in the low dose rate irradiated Fe3%Mn alloy; and (c) the corresponding STEM/HAADF image presented with the STEM/EDS maps, carried out on the part highlighted in red in (b). Fe atoms signal appears in red while Mn atoms signal in green.

Mn-rich clusters analyzed by APT in this sample did not provide reliable results due to low statistics, besides the mismatch in terms of dose (1.2 ± 0.3 dpa instead of 1.9 – 2.3 dpa). It should however be pointed out that the enrichment level is extremely high (up to 56.8 ± 5.2 at.%Mn) compared to the high dose rate condition ($27.7 \pm 5.4 < x$ (at.%Mn) $< 33.8 \pm 2.4$). Extra microstructural and elemental analyses were performed on the FIB-elaborated lamella to investigate spatial correlation between PD clusters and solute clusters. For this purpose, EDS technique in STEM mode was chosen. The FIB lamella was tilted to reach a {100} zone axis. Under these conditions, the electron beam is contained in the habitat plane of two families of <100> dislocation loops. This approach was taken to limit the contribution of the matrix and, thus, to maximize the signal of Mn possibly decorating the loop. Fig. 8.b and 8.c presents qualitatively the results obtained on an edge-on dislocation loop associated to Mn

enrichment. The spatial correlation between dislocation loops and Mn clusters is thereby confirmed. No quantification is given here. Indeed, despite the caution taken during the measurement and even though the sample thickness was less than 100 nm, the dislocation loop signal is still believed to be affected by the matrix signal and thus, misrepresented.

Summary for the Fe3%Mn alloy

Table 3 summarizes all the data obtained during the study of Fe3%Mn irradiated alloy.

Table 3: Results obtained in the Fe3%Mn alloy, regarding PD clusters by TEM and solute clusters by APT, after irradiation at high and low dose rates.

APT data after ion irradiation [a]	**High dose rate**	**Low dose rate**
Mean diameter (nm)	5.0 ± 0.7	Truncated features [b]
Mean number density (x 10^{23} m^{-3})	2.9 ± 0.4	0.17 ± 0.12
Solute content (at.%)	27.7 ± 5.4 < x < 33.8 ± 2.4	Up to 56.8 ± 5.2
Segregated/precipitated atomic fraction	9.5	--
TEM data after ion irradiation	**High dose rate**	**Low dose rate**
Mean diameter (nm)	11 ± 3	<111> : 41 ± 6 <100> : 81 ± 26
Mean number density (x 10^{20} m^{-3})	> 10^{3}	8.2 ± 1.5 [c]

[a] This analysis was performed at a lower depth (~ 1 µm); where the dose does not correspond to the reference dose for this alloy (1.6 – 1.9 dpa). These values are shown on an indicative basis.

[b] Mn-rich clusters cross the edge of the APT volume. Their size is, therefore, not representative of any microstructural feature.

[c] This value include both dislocation loop type (<100> and ½ <111>).

4. Discussion

In this study, TEM and APT techniques have been used complementarily to characterize PD clusters and solute clusters in high and low dose rate irradiated Fe3%Ni and Fe3%Mn undersaturated alloys. Results presented in section 3 demonstrate solute-rich atmospheres and dislocation loops under both irradiation conditions (high and low dose rate) in both alloys. The major objective of this work is to investigate and discuss, as follows, the effects of irradiation dose rate on microstructure and segregation/precipitation in undersaturated FeNi (at a dose of 1.2 – 1.9 dpa) and FeMn (at a dose of 1.9 – 2.3 dpa) model alloys.

1. Segregation/precipitation mechanism

As detailed in the introduction, FeNi and FeMn alloys used in this work contain 3.3at.% of Ni and 2.8at.% of Mn respectively. The alloying element in each material was deliberately chosen higher than their actual content in RPV steels in order to exacerbate solute segregation, thereby emphasizing their

effect on microstructure. Even though solute content is significantly higher in each binary alloy than their actual content in RPV steels, it remains lower than their solubility limit at the temperature of interest (673 K), which is about 6 [12,68–70] and 3.2 at.% [71] in Fe-Ni and Fe-Mn binary systems respectively. Therefore, no thermodynamic driving forces are involved in Ni and Mn clustering process. The clustering of Ni and Mn is not enhanced but induced by irradiation. Consequently, Ni and Mn segregation is expected to occur on microstructural defects. This point is detailed herein for each alloy.

Fe3%Ni alloy

In Fe3%Ni irradiated at high dose rate (5.1 - 6.1 x 10^{-4} dpa.s^{-1}; 1.2 – 1.9 dpa), one can note that the measures of size and number density obtained by TEM and APT are not identical. In terms of size, solute clusters (10 ± 3 nm) are three times larger than dislocation loops (3 ± 1 nm). Considering Ni segregation on a dislocation loop, the diameter of solute cluster measured by APT will naturally be higher than the diameter of the associated loop observed by TEM. A profile was plotted along a Ni-rich cluster in order to evaluate how smooth is the Ni profile. Results are given in Fig. 9. It turns out that the profile is spread over a large distance (~ 25 nm), accounting for such variations in size. Regarding the mismatch in number density, an underestimation by conventional TEM was expected given that imaging resolution is about 1.5 nm. Consequently, small dislocation loops are not visible, leading to a lower dislocation loop density (20 ± 6 x 10^{21} m^{-3}) when compared to that of Ni clusters (14 ± 2 x 10^{22} m^{-3}).

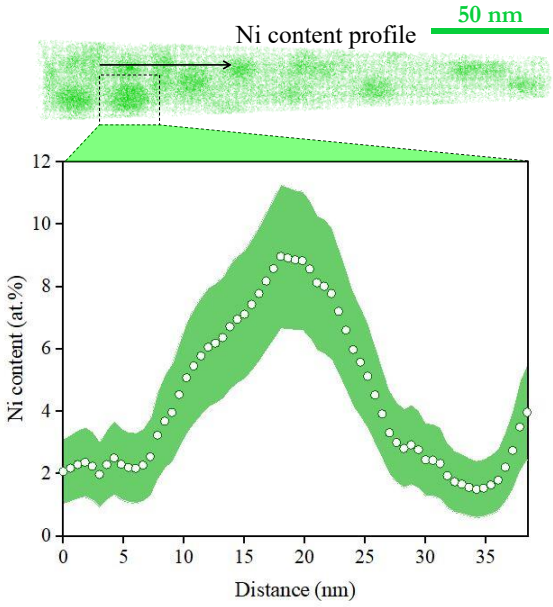

Figure 9: Ni concentration profile plotted along a Ni-rich cluster in the Fe3%Ni alloy irradiated at high dose rate. The solid green area gives the statistical error on the measurement.

Regarding RIS and RIP mechanism in the low dose rate irradiated Fe3%Ni sample (6.1 – 8.2 x 10^{-6} dpa.s^{-1}; 1.2 – 1.9 dpa), readers are encouraged to refer to [67], where comprehensive information is given in detail.

Fe3%Mn alloy

In the Fe3%Mn alloy irradiated at high dose rate (6.9 - 8.8 x 10^{-4} dpa.s^{-1}; 1.9 – 2.3 dpa), contrary to Fe3%Ni irradiated under the same conditions, the diameter of Mn-rich clusters is lower than the one of dislocation loops. This observation is believed to find an explanation in the strong spatial resolution degradation generated by local magnification effects in two-phase alloys when the difference of

evaporation field between precipitates and surrounding matrix is remarkable [64,72–74], as it is the case in Mn-rich clusters in the Fe matrix. Ion trajectories deflection leads to the flattening of the cluster region, where atoms are preferentially field evaporated. Therefore, a direct comparison of Mn-rich clusters and dislocation loops' size is not feasible. However, taking into account that only dislocation loops are present at the depth of interest, the good agreement between their number density and the one of Mn-rich clusters (both > 10^{23} m^{-3}) suggests that these two features are spatially correlated.
In the low dose rate irradiated Fe3%Mn sample (1.2 – 1.5 x 10^{-5} dpa.s^{-1}; 1.9 – 2.3 dpa), a direct evidence for Mn clustering on large dislocation loops was provided by STEM/HAADF and STEM/EDS (Fig. 8.b and 8.c). Large <100> and small ½ <111> dislocation loops, in addition to dislocation network, were observed by TEM, while APT reconstructed volumes revealed the presence of toroidal and linear Mn-rich clusters, substantiating further Mn clustering on dislocation loops and lines.

2. Dose rate effects

In both Fe3%Ni alloy, where the difference in dose rate is around 70 for a same dose of 1.2 - 1.9 dpa, and Fe3%Mn alloy, where the difference in dose rate is around 60 for a same dose of 1.9 – 2.3 dpa, a clear effect of dose rate was observed.

The microstructure was drastically different. At high dose rate in both alloys, small dislocation loops formed in high density. At low dose rate, γ-Fe25%Ni precipitates formed in Fe3%Ni while a dislocation network developed in Fe3%Mn.

APT analyses conducted in Fe3%Ni samples revealed a higher solute segregation/precipitation atomic fraction after low dose rate irradiation, for a same dose. It increased from 5.2% to 66.2%. As reported in the introduction, solute segregation is considered to be caused by PD fluxes driving solute fluxes towards PD sinks. Such a mechanism has been demonstrated to be non-monotonous [20] : Segregation intensity depends on the concentration and mobility of PDs. At high temperatures, PD supersaturation is too low to contribute significantly to solute enrichment on PD sinks. In contrast, at low temperatures, PD supersaturation is high. However, they are not mobile enough so they tend to annihilate and do not play a role in flux coupling. An intermediate range of temperatures where PDs are numerous and mobile enough to drag solutes towards PD sinks optimally exists. Besides, the segregation/precipitation advancement at a given temperature depends on the dose rate [75]. At a lower dose rate (lower supersaturation), the bell curve shifts towards lower temperatures where the supersaturation is also lower. Therefore, operating with a lower dose rate, as it is the case for RPV steels (10^{-10} dpa.s^{-1}), can enhance or reduce the intensity of solute segregation/precipitation. Here, no further calculation was made to compare the precipitation advancement factor since precipitation occurred under one condition only.

In both alloys, solute content measured by APT is higher at low dose rate. Ni and Mn drag by PDs seems to be more efficient under this condition. Since the amplitude of a given irradiation effect, here RIS, is conditioned by the partitioning of defect recombination and elimination on sinks, the elimination rate, which is proportional to the defect concentration times the defect diffusion coefficient times the sink strength, is likely higher at low dose rate. Fig. 2 shows that the low dose rate irradiation produces more small cascades (10 to 100 PDs). One can suppose that cascades with a smaller recombination volume being more numerous under low dose rate irradiation, recombinations may be therefore less frequent under this condition. Besides, time contributes also to solute enrichment given that more time is needed at lower dose rate to reach the same dose. It leads to more significant local enrichment and, to some extent, to precipitation [67].

A last element to be discussed refers to the effect of injected interstitials which can impact diffusion process and the formation of PD clusters. Injected ions, quantified as 0.02 [Fe(at.%)].dpa^{-1} in [76], have been demonstrated to reduce α' precipitation in Fe-Cr alloys. In this paper, while no effect is expected at low dose rate (the analyses were carried out at a depth were no Fe ion is injected), the results obtained in high dose rate irradiated samples must be looked at with more caution. As indicated in section 2.2, the dose is 1.2 – 1.9 dpa and 1.9 – 2.1 dpa in Fe3%Ni and Fe3%Mn alloys respectively, where the injected interstitials over dose ratio is estimated at 6.5 x 10^{-3} and 1.4 x 10^{-2} [Fe(at.%)].dpa^{-1} respectively. An enhancement of mutual recombination together with the creation of a high density of PD sinks (small PD clusters) is therefore expected to be non-negligible. This observation must be kept in mind since the subsequent decrease concentration of PDs, which are required for Ni and Mn atom diffusion, is responsible for a plausible solute redistribution different from the one that would be obtained without injected ions. Therefore, the present results highlighting a lower solute elimination on sinks at high dose rate (less significant solute segregation) may, to a certain extent, be influenced by the add-on PD sinks and the reduction in PD concentration at high dose rate, both leading to a slightly lower solute content in the vicinity of PD sinks.

3. Chemical effects

The comparison of enrichment and segregated/precipitated atomic fractions of Ni and Mn in the Fe3%Ni and Fe3%Mn alloys respectively, under both irradiation conditions, shows that microstructural defects contain more solute elements in the case of the FeMn alloy. These results point out a trend for segregation that is stronger for Mn than Ni in Fe. This observation can be explained by the fact that, as mentioned in the introduction, Mn disposes of two efficient diffusion mechanisms (vacancies and interstitials) while Ni is dragged by vacancies only [29,33].

Despite the fact that Mn enrichment on dislocation loops was substantial, no second phase precipitate was observed. The Fe-Mn phase diagram cannot be taken as a reference for the prediction of phase transformations under irradiation, especially concerning solubility limits. However, this result can be explained by the fact that, contrary to the FeNi system, no intermetallic compound exists in the Fe-Mn binary system [71]. Rather, a miscibility gap can prevail between the α domain and a more concentrated phase. No similar driving force, as in FeNi, for the formation of such a phase acts on the FeMn system. Moreover, the Mn-rich phase, where Mn content exceeds 70 at.%, constitutes a complex phase containing 56 atoms with a lattice parameter equal to 8.877 Å (c=8.873 Å) [77]. The energy required to create such an interface would probably be too high. The fact that we did not find out any second phase in this specimen stands for either the absence of such a phase or the impossibility to detect it using conventional diffraction tools as TEM because of its low volume fraction (low dislocation loop density, 8.2 ± 1.5 x 10^{20} m^{-3}). In the second case, the intensity of diffraction spots related to this phase would be insufficient to be visible by TEM. The investigation of phase transformation should be done by means of a more powerful technique such as high-resolution X-ray diffraction using synchrotron X-rays.

5. Conclusion

The present paper presents the results obtained after self-ion irradiations carried out on two undersaturated ferritic Fe-3.3at.%Ni and Fe-2.8at.%Mn alloys. Two dose rates were used to reach 1.2 – 1.9 dpa in the first material and 1.9 – 2.3 dpa in the second, with a ratio of 70 and 60 respectively.

In the Fe3%Ni alloy, the high dose rate irradiation resulted in the formation of Ni clusters likely associated with small dislocation loops. When decreasing the dose rate by 70, γ-Fe25at.%Ni precipitates formed. Dislocation loops are present only near the surface. The mechanism for radiation

induced precipitation was proposed in another publication [67], suggesting that Ni atoms are dragged towards preexisting dislocation loops by vacancies, until the moment the solubility limit of Ni in Fe is reached locally. The segregated/precipitated atomic fraction is much higher under this condition (66.2%) than after high dose rate irradiation (5.2%). Dose rate effects on Ni precipitation kinetics are thus very strong.

TEM, STEM/EDS and APT characterizations performed on the Fe3%Mn alloy also revealed the presence of Mn-rich clusters associated with dislocation loops, under both irradiation conditions. In the high dose rate irradiated specimen, Mn clusters detected by APT, containing between 27.7 ± 5.4 and 33.8 ± 2.4 at.% of Mn, were flat and oriented along the <100> directions. Their flatness is believed to be due to local magnification effects, as Mn-rich clusters are preferentially field evaporated. In the low dose rate irradiated sample, Mn enrichment was much higher (56.8 ± 5.2 at.%) but no phase transformation was brought out by TEM.

For the first time, a direct comparison of dose rate effects is made on these undersaturated model alloys, where only radiation induced segregation (RIS) can occur. This work reveals that:

1- RIS, taking place in such undersaturated systems, leads to a very high solute enrichment on point defect sinks;
2- At equivalent dose, lower the dose rate modifies the "defect recombination over elimination" ratio and allows solute atoms, coupled with point defects, to benefit from more time to diffuse towards point defect sinks;
3- Solute enrichment is thereby more significant after low dose rate irradiation, to such an extent that unpredicted phase transformations can occur;
4- Extrapolating the results on model alloy to RPV steels strongly suggest an important contribution of the RIS mechanism to the formation of solute clusters. They consequently do not need any thermodynamic driving force to appear and are likely to be maintained by point defect supersaturation;
5- Comparison between both alloys of interest reveals a stronger trend of Mn for segregation. This observation is explained by DFT based calculations demonstrating the possibility for Mn to form Mn-V complexes and mixed Fe-Mn dumbbells, contrary to Ni which is coupled with vacancies only [29,33].

Declaration of interest

The authors declare no conflict of interest.

Acknowledgments

The authors wish to thank JANNuS (Joint Accelerators for Nanoscience and Nuclear Simulation, Saclay) team for performing the ion irradiation and Paul Haghi-Ashtiani from ECP for the help on the FEI Titan microscope. The authors also acknowledge A. Fraczkiewicz from EMSE for providing the material. Alain Barbu and Maylise Nastar also contributed to this work throughout fruitful and stimulating discussions. This work was carried out within the MATMECA consortium and supported by the ANR under contract number ANR-10-EQPX-37. It has benefited from the facilities of the Laboratory MSSMat, CNRS, Centrale Supélec, Université Paris-Saclay, France. This work is supported by the French Network EMIR and funded by SOTERIA (Safe long-term operation of light water reactors based on improved understanding of radiation effects in nuclear structural materials) and by the 'défi NEEDS' (CNRS-CEA-EDF-ANDRA-AREVA-IRSN-BRGM) within the project

SAFETY, and by the GENESIS EQUIPEX Program [PIA, ANR (ANR-11-EQPX- 0020) and Normandie region].

References

1. Auger, P., Pareige, P., Welzel, S. & Duysen, J.-C. V. Synthesis of atom probe experiments on irradiation-induced solute segregation in French ferritic pressure vessel steels. *J. Nucl. Mater.* **280**, 331–344 (2000).
2. Carter, R. G. *et al.* Microstructural characterization of irradiation-induced Cu-enriched clusters in reactor pressure vessel steels. *J. Nucl. Mater.* **298**, 211 – 224 (2001).
3. Miller, M. K., Pareige, P. & Burke, M. G. Understanding Pressure Vessel Steels: An Atom Probe Perspective. *Mater. Charact.* **44**, 235 – 254 (2000).
4. Miller, M. K. *et al.* Evolution of the nanostructure of VVER-1000 {RPV} materials under neutron irradiation and post irradiation annealing. *J. Nucl. Mater.* **385**, 615 – 622 (2009).
5. Pascuet, M. I. *et al.* Solute precipitation on a screw dislocation and its effects on dislocation mobility in bcc Fe. *J. Nucl. Mater.* **519**, 265–273 (2019).
6. Nastar, M. & Soisson, F. 1.18 - Radiation-Induced Segregation. in *Comprehensive Nuclear Materials* (ed. Konings, R. J. M.) 471 – 496 (Elsevier, 2012). doi:10.1016/B978-0-08-056033-5.00035-5.
7. Auger, P., Pareige, P., Akamatsu, M. & Duysen, J.-C. V. Microstructural characterization of atom clusters in irradiated pressure vessel steels and model alloys. *J. Nucl. Mater.* **211**, 194 – 201 (1994).
8. Arakawa, K. & Kiritani, M. Spatial distribution of nucleation of point defect clusters in irradiated metals. *J. Nucl. Mater.* **239**, 1 – 6 (1996).
9. Inoue, H., Muroga, T., Miyamoto, Y. & Yoshida, N. Characteristics of point defects and their clustering processes in Feî—¸Mnî—¸Cr and Feî—¸Mnî—¸Siî—¸Cr alloys. *J. Nucl. Mater.* **191**, 1342 – 1345 (1992).

10. Kiritani, M. *et al.* Formation of vacancy clustered defects from cascade collisions during heavy-ion irradiation and their annihilation by freely-migrating interstitial atoms. *J. Nucl. Mater.* **212**, 192 – 197 (1994).
11. Kojima, S., Yoshiie, T., Hamada, K., Satori, K. & Kiritani, M. Fluctuation effect of point defect reaction on nucleation of interstitial clusters during neutron irradiation. *J. Nucl. Mater.* **191**, 1155 – 1159 (1992).
12. Martin, G. Contribution of dissipative processes to radiation-induced solid-solution instability. *Phys Rev B* **21**, 2122–2130 (1980).
13. Mansur, L. K. Effective diffusion coefficients of point defects in impure materials. *Acta Metall.* **29**, 375 – 381 (1981).
14. Best, S. E. & Russell, K. C. Irradiation-altered precipitation in Fe-Ni-C alloys. *J. Nucl. Mater.* **133**, 599 – 603 (1985).
15. Terentyev, D., Olsson, P., Malerba, L. & Barashev, A. V. Characterization of dislocation loops and chromium-rich precipitates in ferritic ironÃ¢â‚¬â€œchromium alloys as means of void swelling suppression. *J. Nucl. Mater.* **362**, 167 – 173 (2007).
16. Yoshiie, T. & Kiritani, M. Destination of point defects and microstructural evolution under collision cascade damage. *J. Nucl. Mater.* **271Ã¢â‚¬â€œ272**, 296 – 300 (1999).
17. Wagner, A. *et al.* Effect of neutron flux on the characteristics of irradiation-induced nanofeatures and hardening in pressure vessel steels. *Acta Mater.* **104**, 131 – 142 (2016).
18. Watanabe, H., Masaki, S., Masubuchi, S., Yoshida, N. & Dohi, K. Effects of Mn addition on dislocation loop formation in {A533B} and model alloys. *J. Nucl. Mater.* **439**, 268 – 275 (2013).
19. Jourdan, T., Bencteux, G. & Adjanor, G. Efficient simulation of kinetics of radiation induced defects: A cluster dynamics approach. *J. Nucl. Mater.* **444**, 298 – 313 (2014).
20. Meslin, E., Radiguet, B., Pareige, P. & Barbu, A. Kinetic of solute clustering in neutron irradiated ferritic model alloys and a French pressure vessel steel investigated by atom probe tomography. *J. Nucl. Mater.* **399**, 137 – 145 (2010).
21. Fujii, K., Ohkubo, T. & Fukuya, K. Effects of solute elements on irradiation hardening and microstructural evolution in low alloy steels. *J. Nucl. Mater.* **417**, 949 – 952 (2011).

22. Ishida, I. *et al.* Analysis of the sub-cascade structure in copper produced by ion irradiations. *J. Nucl. Mater.* **179**, 913 – 916 (1991).
23. Mathon, M. H. *et al.* Experimental study and modelling of copper precipitation under electron irradiation in dilute FeCu binary alloys. *J. Nucl. Mater.* **245**, 224 – 237 (1997).
24. Soisson, F., Barbu, A. & Martin, G. Monte Carlo simulations of copper precipitation in dilute iron-copper alloys during thermal ageing and under electron irradiation. *Acta Mater.* **44**, 3789 – 3800 (1996).
25. Liu, C. L., Odette, G. R., Wirth, B. D. & Lucas, G. E. A lattice Monte Carlo simulation of nanophase compositions and structures in irradiated pressure vessel Fe-Cu-Ni-Mn-Si steels. *Mater. Sci. Eng. A* **238**, 202 – 209 (1997).
26. Odette, G. R. & Wirth, B. D. A computational microscopy study of nanostructural evolution in irradiated pressure vessel steels. *J. Nucl. Mater.* **251**, 157 – 171 (1997).
27. Styman, P. D., Hyde, J. M., Wilford, K., Morley, A. & Smith, G. D. W. Precipitation in long term thermally aged high copper, high nickel model RPV steel welds. *Prog. Nucl. Energy* **57**, 86 – 92 (2012).
28. Styman, P. D. *et al.* Post-irradiation annealing of Ni–Mn–Si-enriched clusters in a neutron-irradiated RPV steel weld using Atom Probe Tomography. *J. Nucl. Mater.* **459**, 127 – 134 (2015).
29. Messina, L., Schuler, T., Nastar, M., Marinica, M.-C. & Olsson, P. Solute diffusion by self-interstitial defects and radiation-induced segregation in ferritic Fe-X (X= Cr, Cu, Mn, Ni, P, Si) dilute alloys. *ArXiv Prepr. ArXiv191011440* (2019).
30. Odette, G. R. Radiation Induced Microstructural Evolution in Reactor Pressure Vessel Steels. *MRS Proc.* **373**, (1994).
31. Odette, G. R. & Lucas, G. E. Recent progress in understanding reactor pressure vessel steel embrittlement. *Radiat. Eff. Defects Solids* **144**, 189–231 (1998).
32. Lambrecht, M. *et al.* On the correlation between irradiation-induced microstructural features and the hardening of reactor pressure vessel steels. *J. Nucl. Mater.* **406**, 84 – 89 (2010).
33. Messina, L., Nastar, M., Sandberg, N. & Olsson, P. Systematic electronic-structure investigation of substitutional impurity diffusion and flux coupling in bcc iron. *Phys. Rev. B* **93**, (2016).

34. Jacob, A., Domain, C., Adjanor, G., Todeschini, P. & Povoden-Karadeniz, E. Thermodynamic modeling of G-phase and assessment of phase stabilities in reactor pressure vessel steels and cast duplex stainless steels. *J. Nucl. Mater.* 152091 (2020).
35. Odette, G. R. & Nanstad, R. K. Predictive reactor pressure vessel steel irradiation embrittlement models: Issues and opportunities. *JOM* **61**, 17–23 (2009).
36. Miller, M. K., Powers, K. A., Nanstad, R. K. & Efsing, P. Atom probe tomography characterizations of high nickel, low copper surveillance RPV welds irradiated to high fluences. *J. Nucl. Mater.* **437**, 107 – 115 (2013).
37. Odette, G. R. *High Fluency Low Flux Embrittlement Models of LWR Reactor Pressure Vessel Embrittlement and a Supporting Database from the UCSB ATR-2 Irradiation Experiment*. (2017). doi:10.2172/1346148.
38. Almirall, N. *et al.* Precipitation and hardening in irradiated low alloy steels with a wide range of Ni and Mn compositions. *Acta Mater.* **179**, 119–128 (2019).
39. Sprouster, D. J. *et al.* Structural characterization of nanoscale intermetallic precipitates in highly neutron irradiated reactor pressure vessel steels. *Scr. Mater.* **113**, 18 – 22 (2016).
40. Wells, P. B. *et al.* Evolution of manganese–nickel–silicon-dominated phases in highly irradiated reactor pressure vessel steels. *Acta Mater.* **80**, 205–219 (2014).
41. Shu, S., Wells, P. B., Odette, G. R. & Morgan, D. A kinetic lattice Monte Carlo study of post-irradiation annealing of model reactor pressure vessel steels. *J. Nucl. Mater.* **524**, 312–322 (2019).
42. Almirall, N. *et al.* On the elevated temperature thermal stability of nanoscale Mn-Ni-Si precipitates formed at lower temperature in highly irradiated reactor pressure vessel steels. *Sci. Rep.* **9**, 1–12 (2019).
43. Meslin, E., Radiguet, B., Pareige, P., Toffolon, C. & Barbu, A. Irradiation-Induced Solute Clustering in a Low Nickel FeMnNi Ferritic Alloy. *Exp Mech* **51**, 1453–1458 (2011).
44. Ngayam-Happy, R., Becquart, C. S., Domain, C. & Malerba, L. Formation and evolution of MnNi clusters in neutron irradiated dilute Fe alloys modelled by a first principle-based {AKMC} method. *J. Nucl. Mater.* **426**, 198 – 207 (2012).

45. Bonny, G. *et al.* On the thermal stability of late blooming phases in reactor pressure vessel steels: An atomistic study. *J. Nucl. Mater.* **442**, 282 – 291 (2013).
46. Todeschini, P. *et al.* Revision of the irradiation embrittlement correlation used for the EDF RPV fleet. *RGN* 29–42 (2011) doi:10.1051/rgn/20111029.
47. Hirsch, P. B., Howie, A., Nicholson, R., Pashley, D. & Whelan, M. J. Electron microscopy of thin crystals. *1965 549 P BUTTERWORTH INC 7300 PEARL Str. Wash. C 20014* (1966).
48. Serruys, Y. *et al.* JANNUS: A multi-irradiation platform for experimental validation at the scale of the atomistic modelling. *J. Nucl. Mater.* **386–388**, 967 – 970 (2009).
49. Beck, L. *et al.* Ion irradiation and radiation effect characterization at the JANNUS-Saclay triple beam facility. *J. Mater. Res.* **30**, 1183–1194 (2015).
50. Stoller, R. E. [ORNL], Toloczko, M. [Pacific N. N. L. (PNNL)], Was, G. [University of M., Certain, A. [Pacific N. N. L. (PNNL)] & Dwaraknath, S. [University of M. On the Use of SRIM/TRIM for Computing Radiation Damage Exposure. *Nucl. Instrum. Methods Phys. Res. Sect. B Beam Interact. Mater. At.* (2013) doi:10.1016/j.nimb.2013.05.008.
51. Kinchin, G. H. & Pease, R. S. The Displacement of Atoms in Solids by Radiation. *Rep. Prog. Phys.* **18**, 1–51 (1955).
52. Borschel, C. & Ronning, C. Ion beam irradiation of nanostructures - A 3D Monte Carlo simulation code. *Nucl. Instrum. Methods Phys. Res. Sect. B Beam Interact. Mater. At.* **269**, 2133–2138 (2011).
53. Crocombette, J.-P. & Wambeke, C. Quick calculation of damage for ion irradiation: implementation in Iradina and comparisons to SRIM. (2019).
54. Jenkins, M. L. & Kirk, M. A. *Characterisation of Radiation Damage by Transmission Electron Microscopy*. (CRC Press, 2000).
55. Howie, A. & Whelan, M. J. Diffraction contrast of electron microscope images of crystal lattice defects. III. Results and experimental confirmation of the dynamical theory of dislocation image contrast. *Proc. R. Soc. Lond. Ser. Math. Phys. Sci.* **267**, 206–230 (1962).
56. Prokhodtseva, A., DÃ©camps, B., Ramar, A. & SchÃ¤ublin, R. Impact of He and Cr on defect accumulation in ion-irradiated ultrahigh-purity Fe(Cr) alloys. *Acta Mater.* **61**, 6958 – 6971 (2013).

57. Egerton, R. F. Electron energy-loss spectroscopy in the TEM. *Rep. Prog. Phys.* **72**, 016502 (2009).

58. Watanabe, M. & Williams, D. B. The quantitative analysis of thin specimens: a review of progress from the Cliff-Lorimer to the new ζ-factor methods. *J. Microsc.* **221**, 89–109 (2006).

59. Gault, B., Moody, M., Cairney, J. & Ringer, S. *Atom Probe Microscopy*. (Springer New York, 2012). doi:10.1007/978-1-4614-3436-8.

60. Lefebvre, W., Vurpillot, F. & Sauvage, X. *Atom Probe Tomography: Put Theory Into Practice*. (Academic Press, 2016).

61. Hyde, J. M. *et al.* Analysis of Radiation Damage in Light Water Reactors: Comparison of Cluster Analysis Methods for the Analysis of Atom Probe Data. *Microsc. Microanal.* **23**, 366–375 (2017).

62. Müller, E. W. Field Desorption. *Phys Rev* **102**, 618–624 (1956).

63. Tsong, T. Field ion image formation. *Surf. Sci.* **70**, 211–233 (1978).

64. Vurpillot, F., Bostel, A. & Blavette, D. Trajectory overlaps and local magnification in three-dimensional atom probe. *Appl. Phys. Lett.* **76**, 3127–3129 (2000).

65. Mouton, I. Study and modelling of self-organized nanostructure in Ge-Mn thin film. (Université de Rouen, 2014).

66. Loretto, M. H. & Smallman, R. E. *Defect analysis in electron microscopy*. (Chapman and Hall, 1975).

67. Belkacemi, L. T., Meslin, E., Décamps, B., Radiguet, B. & Henry, J. Radiation-induced bcc-fcc phase transformation in a Fe3%Ni alloy. *Acta Mater.* **161**, 61–72 (2018).

68. Murphy, S. M. Instabilities in concentrated alloys under irradiation. *Philos. Mag. A* **58**, 417–433 (1988).

69. Garner, F. A., Brager, H. R., Dodd, R. A. & Lauritzen, T. Ion-induced spinodal-like decomposition of Fe-Ni-Cr invar alloys. *Nucl. Instrum. Methods Phys. Res. Sect. B Beam Interact. Mater. At.* **16**, 244 – 250 (1986).

70. Kenik, E. A. Elemental inhomogeneities developed in stainless steels by radiation-induced segregation. *J. Nucl. Mater.* **205**, 317 – 323 (1993).

71. Witusiewicz, V. T., Sommer, F. & Mittemeijer, E. J. Reevaluation of the Fe-Mn phase diagram. *J. Phase Equilibria Diffus.* **25**, 346–354 (2004).
72. Miller, M. K. & Hetherington, M. G. Local magnification effects in the atom probe. *Surf. Sci.* **246**, 442–449 (1991).
73. Miller, M. K., Cerezo, A., Hetherington, M. G. & FRS, G. D. W. S. *Atom Probe Field Ion Microscopy*. (Oxford University Press, 1996).
74. De Geuser, F. *et al.* An improved reconstruction procedure for the correction of local magnification effects in three-dimensional atom-probe. *Surf. Interface Anal.* **39**, 268–272 (2007).
75. Okamoto, P. R. & Rehn, L. E. Radiation-induced segregation in binary and ternary alloys. *J. Nucl. Mater.* **83**, 2 – 23 (1979).
76. Tissot, O., Pareige, C., Meslin, E., Décamps, B. & Henry, J. Influence of injected interstitials on α′ precipitation in Fe–Cr alloys under self-ion irradiation. *Mater. Res. Lett.* **5**, 117–123 (2017).
77. Hobbs, D., Hafner, J. & Spıɪfmmode \textbackslashchecks\textbackslashelse š\textbackslashfiák, D. Understanding the complex metallic element Mn. I. Crystalline and noncollinear magnetic structure of \textbackslashensuremath\textbackslashalpha-Mn. *Phys Rev B* **68**, 014407 (2003).